PHYSICAL REVIEW B **66**, 174427 (2002)

Heisenberg dimer single molecule magnets in a strong magnetic field

Dmitri V. Efremov* and Richard A. Klemm†
Max-Planck-Institut für Physik komplexer Systeme, Nöthnitzer Strasse 38, D-01187 Dresden, Germany

(Received 21 June 2002; published 15 November 2002)

We calculate the static and dynamic properties of single crystal, single molecule magnets consisting of equal spin $S=1/2$ or 5/2 dimers. The spins in each dimer interact with each other via the Heisenberg exchange interaction and with the magnetic induction **B** via the Zeeman interaction, and interdimer interactions are negligible. For antiferromagnetic couplings, the static magnetization and specific heat exhibit interesting low-temperature T and strong **B** quantum effects. We calculate the frequency spectrum of the Fourier transform of the real part of the time autocorrelation function $\mathcal{C}_{11}(t)$ for arbitrary T, **B**, and compare our results with those obtained for classical spins. We also calculate the inelastic neutron magnetic dynamical structure factor $S(\mathbf{q},\omega)$ at arbitrary T, **B**.

DOI: 10.1103/PhysRevB.66.174427 PACS number(s): 75.10.Hk, 05.20.−y, 75.75.+a, 05.45.−a

I. INTRODUCTION

Recently, there has been a considerable interest in the physics of single molecule magnets (SMM's), or magnetic molecules.[1–12] These consist of small clusters of magnetic ions embedded within a nonmagnetic ligand group, which may crystallize into large, well-ordered single crystals of sufficient quality for neutron scattering studies. Usually, the spins within a single molecule interact mainly via the Heisenberg exchange interaction. In the simplest SMM's, $V2$, Cu2, two examples of Yb2, Cr2, and four examples of Fe2, the magnetic cores of the molecules consist of dimers of spin $S=1/2$ V^{4+}, Cu^{2+}, or Yb^{3+}, $S=3/2$ Cr^{3+}, or $S=5/2$ Fe^{3+} spins, respectively.[5,8–11] Low-field magnetization, nuclear magnetic resonance (NMR) and electron paramagnetic resonance (EPR) experiments, and zero-field inelastic neutron scattering experiments were made on some of these dimers.[5–12] Theoretically, zero-field results for the time dependence of the autocorrelation function of the quantum $S=1/2$ and $S=5/2$ dimers were presented.[13]

Here we study the simplest model of interacting Heisenberg spins in a magnetic field **H**. We assume only two spins, which interact with each other via the ordinary Heisenberg exchange interaction J, and also with a constant magnetic induction **B** induced by the application of **H**. For simplicity, we limit our discussion to the spin values $S=1/2$ and $S=5/2$.

We first evaluate the static magnetization **M** and specific heat C_V as functions of T and **B**. We find that for ferromagnetic (FM) exchange couplings $J>0$, both **M** and C_V behave at low T as for a single paramagnetic ion with spin $2S$, qualitatively similar to that expected from a classical treatment. For antiferromagnetic (AFM) exchange couplings $J<0$, however, for $k_BT\ll|J|$, the low-T results are very nonclassical, even for $S=5/2$. **M**(**B**) for the AFM spin-S dimer exhibits $2S$ discrete steps, reminiscent of the transverse conductivity in the integer quantum Hall effect. In addition, $C_V(T,B)$ exhibits $2S$ doublet peaks centered about the corresponding magnetization step fields, the splitting of which is proportional to T.

At arbitrary T,**B**, we then evaluate the real part of the time autocorrelation function $\mathcal{C}_{11}(t)$, and focus upon its Fourier transform $\tilde{\mathcal{C}}_{11}(\omega)$, which is applicable to inelastic neutron scattering experiments. For $\mathbf{B}=0$, $\tilde{\mathcal{C}}_{11}(\omega)$ for the spin-S dimer has $4S+1$ equally-spaced modes with frequencies $\omega^0_{S,n}=n|J|$, where $n=-2S,-2S+1,\dots,2S-1,2S$. Depending upon T and the sign of J, the relative importance of these modes varies significantly. For $\mathbf{B}\neq 0$, each of these $\omega^0_{S,n}$ modes is split into 3 modes. We study the T and **B** dependence of the most important of these modes for $S=1/2$ and 5/2, for both FM and AFM exchange couplings. For the FM case, only a few modes are important at low T, and their relative strength is nearly independent of $|B|$. For the AFM case, however, the situation is more complicated, as many modes can be important at rather low T, and their relative importance shifts with $|B|$. For comparison, we also present the analogous results for classical spins. Finally, at arbitrary T,**B**, we evaluate the magnetic dynamical structure factor $S(\mathbf{q},\omega)$ measurable with inelastic neutron scattering, and identify a method by which it can measure $\tilde{\mathcal{C}}_{11}(\omega)$.

II. THERMODYNAMIC PROPERTIES

A. Partition function

Here we derive the partition function Z for the quantum dimer for $\mathbf{B}\neq 0$, with spin $i=1,2$ represented by the operator $\mathbf{S}_i$, and set $\hbar=1$ for convenience. The Hamiltonian is

$$\mathcal{H}=-J\mathbf{S}_1\cdot\mathbf{S}_2-\gamma\mathbf{B}\cdot(\mathbf{S}_1+\mathbf{S}_2), \tag{1}$$

where $\gamma=g\mu_B$ is the gyromagnetic ratio. Letting the total spin operator $\mathbf{s}=\mathbf{S}_1+\mathbf{S}_2$, $\mathcal{H}$ is rewritten as

$$\mathcal{H}=-J(\mathbf{s}^2-\mathbf{S}_1^2-\mathbf{S}_2^2)/2-\gamma Bs_z. \tag{2}$$

The dimer quantum states are then indexed by the quantum numbers s and m, where

$$\mathbf{s}^2|sm\rangle=s(s+1)|sm\rangle, \tag{3}$$

$$s_z|sm\rangle=m|sm\rangle, \tag{4}$$

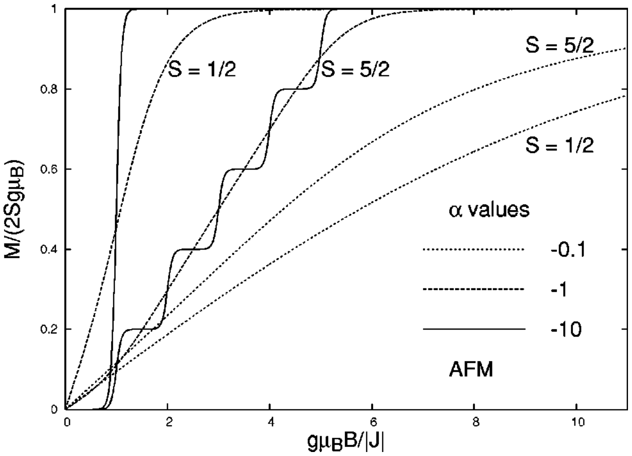

FIG. 1. Plots of the static magnetization M normalized to $2Sg\mu_B$ versus $\overline{B}=g\mu_BB/|J|$ for the AFM $S=1/2$ and $S=5/2$ dimers at $\alpha=J/(2k_BT)=-0.1,-1,-10$, as indicated.

and since $\mathbf{S}_i^2|sm\rangle=S(S+1)|sm\rangle$, where $S(S+1)$ is a constant for all measurable quantities, we drop the terms proportional to $\mathbf{S}_1^2$ and $\mathbf{S}_2^2$ in $\mathcal{H}$ for convenience.

Letting $\beta=1/(k_BT)$, $\alpha=\beta J/2$, $b=\beta\gamma B$, and $\overline{B}=g\mu_BB/|J|=b/(2|\alpha|)$, the partition function $Z=\mathrm{Tr}[\exp(-\beta\mathcal{H})]$ for the Heisenberg dimer is simply

$$Z=\sum_{s=0}^{2S}\sum_{m=-s}^{s}e^{\alpha s(s+1)+bm}=\sum_{s=0}^{2S}\mathcal{D}_s(\alpha,b), \tag{5}$$

where

$$\mathcal{D}_S(\alpha,b)=e^{\alpha s(s+1)}\frac{\sinh[(2s+1)b/2]}{\sinh(b/2)}. \tag{6}$$

B. Magnetization

The magnetization $\mathbf{M}=\beta^{-1}\vec{\nabla}_{\mathbf{B}}(\ln Z)$ for the spin-S dimer in a field is then easily found to be

$$\mathbf{M}(\alpha,b)=\frac{\gamma\hat{\mathbf{B}}}{Z}\sum_{s=0}^{2S}\mathcal{D}_s(\alpha,b)B_s(b) \tag{7}$$

$$\equiv\gamma\hat{\mathbf{B}}\langle B_s(b)\rangle, \tag{8}$$

where

$$B_s(b)=(s+1/2)\coth[(s+1/2)b]-\frac{1}{2}\coth(b/2) \tag{9}$$

is the standard Brillouin function for a spin-s paramagnet in a magnetic field. We note that $\langle\ \dots\ \rangle$ represents a thermodynamic average over the dimer quantum s values, evaluated using the weighting function $\mathcal{D}_s(\alpha,b)$.

In Fig. 1, we plotted $M/(2Sg\mu_B)$ as a function of $\overline{B}$ for the AFM $S=5/2$ and $S=1/2$ dimers at $\alpha=-0.1,-1$, and -10, respectively. At high $k_BT/|J|$ ($|\alpha|\ll 1$), the dotted curves for $\alpha=-0.1$, $S=1/2$, 5/2 are smooth functions of $\overline{B}$, not too different from the analogous results obtained for classical spins. At $\alpha=-1$, the dashed curves remain smooth, but are shifted over to smaller field values, with hints of a kink just below the saturation magnetization value. Most interesting are the low-T effects. At $\alpha=-10$, M has $2S$ steps at integral values of $\overline{B}$, as shown by the solid curves for $S=1/2$,5/2 in Fig. 1. Since these steps are thermodynamic, they are reversible. However, a measurement at fixed B near to a step value can lead to interesting, nonmonotonic behavior of $M(T)$ at low T.

These thermodynamic steps in M are a consequence of quantum level crossing due to the strong B.[3] The energy E_{sm} of the state $|sm\rangle$ is given by

$$E_{sm}=-Js(s+1)-m\widetilde{B}. \tag{10}$$

where $\widetilde{B}=\gamma B$ and $\overline{B}=\widetilde{B}/|J|$. For the AFM case, $J=-|J|$, the lowest energy state for each s value is $E_{sm,\mathrm{min}}=E_{ss}$. The difference in energy between the lowest energy state with quantum number s and that with the next highest quantum number, $s+1$, is then

$$\Delta E_{ss}=E_{s+1,s+1}-E_{ss}=|J|(s+1-|\overline{B}|), \tag{11}$$

which vanishes at $|\overline{B}|=s+1$. For $S=1/2$, there will only be one step, as this crossing can only occur between states corresponding to the $s=0$ and $s=1$ quantum numbers. Similarly, for $S=5/2$, there will be 5 level crossings, corresponding to $s=0,\dots,4$.

For the FM case, the situation is rather boring by comparison. We found that for both $S=1/2$,5/2, $M(\alpha,b)/\gamma$ is closely approximated by $B_{2S}(b)$. For $\alpha=0.1$, this approximation is accurate to a few percent, but for $\alpha=10$, the corresponding curves for M and B_{2S} are indistinguishable. This is because the $s=2S$ term in both the numerator and the denominator of $\langle B_s\rangle$ is dominant for $J>0$.

C. Specific heat

The specific heat C_V is given by

$$k_BT^2C_V=\frac{\partial^2\ln Z}{\partial\beta^2}, \tag{12}$$

leading to

$$\begin{aligned}C_V/k_B={}&b^2[\langle s(s+1)\rangle-\coth(b/2)\langle B_s(b)\rangle-\langle B_s(b)\rangle^2]\\&+2\alpha b[\langle s(s+1)B_s(b)\rangle-\langle B_s(b)\rangle\langle s(s+1)\rangle]\\&+\alpha^2[\langle[s(s+1)]^2\rangle-\langle s(s+1)\rangle^2].\end{aligned} \tag{13}$$

In numerical evaluations of C_V, we checked that Boltzmann's law, $\int_0^\infty dTC_V/T=2k_B\ln(2S+1)$, is satisfied. As for the FM M, C_V for the FM spin-S dimer is rather boring. It is closely approximated by the $s=2S$ terms in each of the sums. In this approximation, only the first term proportional to b^2 survives, so C_V reduces to the standard Schottky result for a spin $2S$-paramagnet,

$$C_V/k_B\overset{\rightarrow}{\alpha\gg}1C_{2S}(b) \tag{14}$$

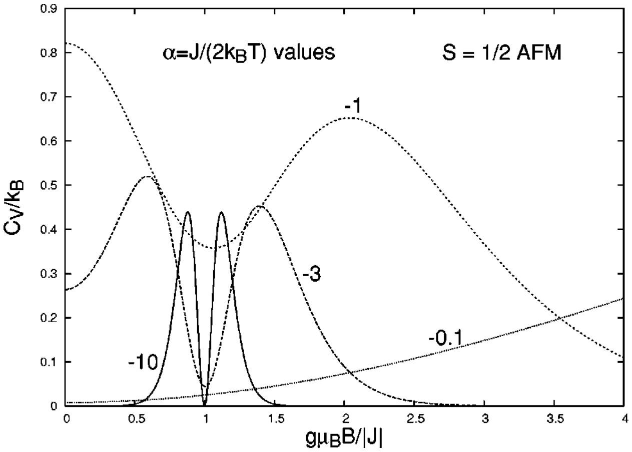

FIG. 2. Plots of C_V/k_B versus $\overline{B}$ at $\alpha=-0.1,-1,-3,-10$, as indicated, for the $S=1/2$ AFM dimer.

$$=b^2\left(2S(2S+1)+\frac{1}{4}\coth^2(b/2)\right.$$

$$\left.-(2S+1/2)^2\coth^2[(2S+1/2)b]\right). \qquad (15)$$

Numerically, for $S=5/2$, the FM C_V is nearly indistinguishable from $C_{2S}(b)$ for $\alpha\geqslant 1$. We note that $C_{2S}(b)$ grows as $2S(2S+1)b^2/3$ for $b\ll 1$, decays as $b^2\exp(-b)$ for $b\gg 1$, and has a maximum for $b\approx 1$. For $S=5/2$, the maximum occurs at $b\approx 0.78$.

On the other hand, C_V for the AFM spin-S dimer is much more interesting. In Figs. 2 and 3, we plotted C_V/k_B versus $\overline{B}$ at $\alpha=-0.1,-1,-3,-10$, for dimers of spin $S=1/2$ and 5/2, respectively. The curves for $\alpha=-0.1$ have broad maxima at fields too high to appear in these figures. But, as T is lowered to $\alpha=-1$, Fig. 2 illustrates that this broad maximum develops into two peaks centered at $\overline{B}\approx 0,2$, respectively. Then, as T is lowered further, C_V for $S=1/2$ becomes two well-defined peaks symmetrically centered about $\overline{B}=1$, with a splitting between them proportional to T.

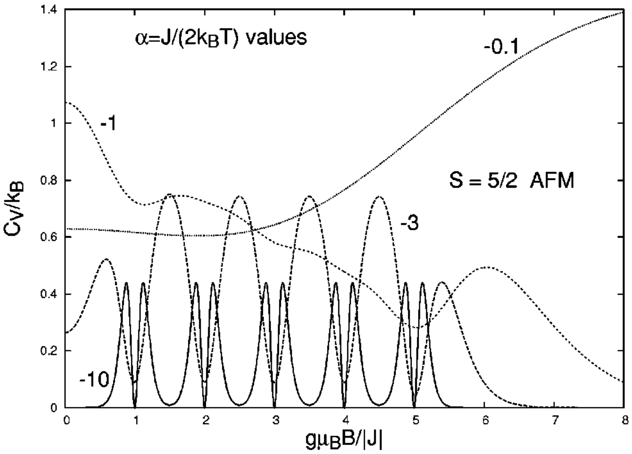

FIG. 3. Plots of C_V/k_B versus $\overline{B}$ at $\alpha=-0.1,-1,-3,-10$, as indicated, for the $S=5/2$ AFM dimer.

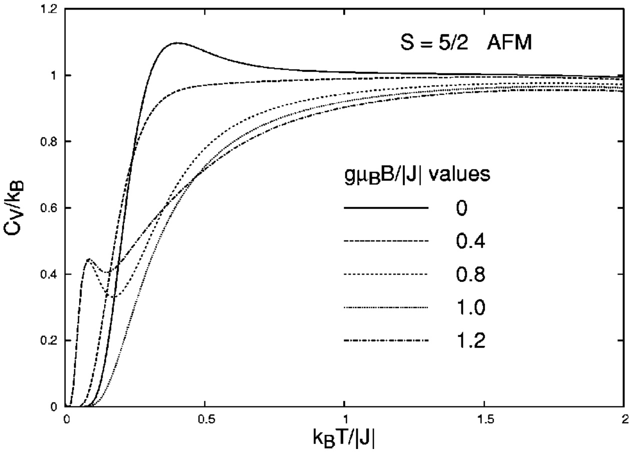

FIG. 4. Plots of C_V/k_B versus $k_BT/|J|$ at $\overline{B}=0,0.4,0.8,1.0,1.2$, as indicated for the $S=5/2$ AFM dimer.

In Fig. 3, the analogous AFM C_V for $S=5/2$ is shown. For $\alpha=-1$, instead of two broad peaks, as in Fig. 2, for $S=5/2$ there is an irregular pattern resulting from many accessible energy levels. The situation becomes clearer at $\alpha=-3$, with six rather symmetric peaks roughly centered at half-integral values of $\overline{B}$. However, as for $S=1/2$, the low-T limiting behavior is not reached until $\alpha=-10$. For $S=5/2$, Fig. 3 shows that C_V consists of five double peaks symmetrically centered about $\overline{B}=s+1$ for $s=0,\ldots,4$, and nearly vanishes at those points.

We note that this multiplicity of double peaks at low T is also a consequence of quantum level crossing. At low T, the energy difference between the two lowest states is given by Eq. (11). At the exact level crossing, these levels are degenerate, leading to an exponentially small value of C_V $[\propto\exp(2\alpha)]$. Just away from these points, excitations from the ground state to the first excited state can occur for $k_BT\gtrsim|J||s+1-|\overline{B}||$. This should lead to a peak on each side of the level crossing points, with a splitting $\Delta\overline{B}$ of the double peaks approximately equal to $1/|\alpha|$. From the data in Figs. 2 and 3 for $|\alpha|=3,10$, the splitting is $\approx 2.4/|\alpha|$, which is $\propto T$, but 2.4 times as large as in the above crude estimate.

We remark that the $2S$ double peak structures in C_V shown in Figs. 2 and 3 comprise a new quantum effect. Although it may be difficult to increase B to 40 T while holding T fixed at $\lesssim 1$ K, it might be easier to lower T in a fixed, strong B. From Figs. 2 and 3, for $\overline{B}$ fixed at 0.8 or 1.2, nonmonotonic $C_V(T)$ behavior upon lowered T is predicted. However, at $\overline{B}=1$, the behavior at low T is very different, as C_V at $\alpha=-10$ is vanishingly small. This striking sensitivity to the precise value of B is pictured in Fig. 4 for $S=5/2$. In Fig. 4, for $k_BT/|J|>1$, the T, B dependencies of C_V are monotonic. Aside from the rather ordinary peak for $B=0$, the unusual behavior is illustrated by comparing the curves for $\overline{B}=0.8,1.0,1.2$ for $k_BT/|J|<0.5$ The curves for $\overline{B}=0.8,1.2$ both have peaks at low T, but the curve for the intermediate value $\overline{B}=1.0$ does not. This highly sensitive dependence of C_V upon T,B is a new quantum level crossing effect.

III. SPIN DYNAMICS

We now evaluate the time autocorrelation function for both quantum and classical spin dimers for $\mathbf{B}\neq 0$.

A. Quantum spin dynamics

The time evolution of quantum spins is given by the commutator of the spin operator with the Hamiltonian,

$$i\dot{\mathbf{S}}_i(t)=[\mathbf{S}_i,\mathcal{H}], \tag{16}$$

$$\mathbf{S}_i=\exp(it\mathcal{H})\mathbf{S}_i(0)\exp(-it\mathcal{H}). \tag{17}$$

It is easiest in the quantum case just to keep the time dependence in this form, and then to let $\mathcal{H}$ operate on the eigenstates in the matrix elements of the correlation function. The total spin operators $\mathbf{s}^2$ and s_z are independent of t.

B. Classical spin dynamics

The two classical spins $\mathbf{S}_i(t)$ each precess according to classical Heisenberg dynamics,

$$\dot{\mathbf{S}}_i=J\mathbf{S}_i\times\mathbf{S}+\gamma\mathbf{S}_i\times\mathbf{B}, \tag{18}$$

where $|\mathbf{S}_i(t)|=1$, for $i=1,2$, $\mathbf{S}=\mathbf{S}_1+\mathbf{S}_2$, leading to

$$\dot{\mathbf{S}}=\gamma\mathbf{S}\times\mathbf{B}. \tag{19}$$

Hence, the total spin **S** precesses about **B**, and the $\mathbf{S}_i$ precess about both **B** and **S**. The solution to these equations is given in the Appendix.

IV. TIME CORRELATION FUNCTIONS

A. Quantum spins

In this section, we evaluate the time correlation functions for quantum spins with general spin value S. Here we calculate the time autocorrelation function for the quantum dimer. For easy comparison with the classical results, we normalize the correlation functions such that $\mathrm{Re}\,\mathcal{C}_{11}(0)=1$.[13] Then $\mathcal{C}_{11}(t)=\langle\mathbf{S}_1(t)\cdot\mathbf{S}_1(0)\rangle$, or

$$\mathcal{C}_{11}(t)=\sum_{s=0}^{2S}\sum_{m=-s}^{s}\langle sm|e^{i\mathcal{H}t}\mathbf{S}_1(0)e^{-i\mathcal{H}t}\cdot\mathbf{S}_1(0)\times e^{-\beta\mathcal{H}}|sm\rangle/D, \tag{20}$$

$$=\sum_{s,m}\sum_{s',m'}\sum_{\alpha=1}^{3}e^{it(E_{sm}-E_{s'm'})}e^{-\beta E_{sm}}\times|\langle sm|S_{1\alpha}|s'm'\rangle|^2/D, \tag{21}$$

$$-\beta E_{sm}=\alpha s(s+1)+bm, \tag{22}$$

$$D=S(S+1)Z, \tag{23}$$

where Z is given by Eq. (5). In Eq. (21), the expectation values are related to Clebsch-Gordon coefficients.

For quantum spins, the near-neighbor correlation function and the autocorrelation function are related by the sum rule,

$$\langle s_z^2\rangle+\langle\mathbf{s}^2-s_z^2\rangle\cos(\tilde{B}t)=\frac{1}{2}\langle\mathbf{s}(t)\cdot\mathbf{s}(0)+\mathbf{s}(0)\cdot\mathbf{s}(t)\rangle=2S(S+1)\mathrm{Re}[\mathcal{C}_{12}(t)+\mathcal{C}_{11}(t)], \tag{24}$$

where $\mathcal{C}_{12}(t)$ is normalized as is $\mathcal{C}_{11}(t)$. The thermal averages $\langle\mathbf{s}^2\rangle$ and $\langle s_z^2\rangle$ can be written in the notation of Eqs. (6)–(9) as $\langle s(s+1)\rangle$ and $\langle s(s+1)\rangle-\coth(b/2)\langle B_s(b)\rangle$, respectively.

B. Classical spins

It is interesting to compare the quantum time correlation functions with those obtained from classical spin dynamics. For classical spin dimers, one solves the equations of motion of the spins directly, taking the length of each spin to be unity. We first solve Eq. (19) for $\mathbf{S}(t)$, and then Eq. (18) to obtain the $\mathbf{S}_i(t)$. We then evaluate the classical autocorrelation function $\mathcal{C}_{11}(t)=\langle\mathbf{S}_1(t)\cdot\mathbf{S}_1(0)\rangle$ by averaging over the length S $(0\leqslant S\leqslant 2)$ of the total spin, the angle θ between **S** and **B**, and the angle ϕ_0 describing the initial relative configuration of $\mathbf{S}_1$ and $\mathbf{S}_2$, and by requiring $\mathcal{C}_{11}(0)=1$. Since the procedure is analogous to that used for the four-spin ring,[14] the results are given in the Appendix. Here we only remark that the classical correlation functions also must satisfy a sum rule,

$$\frac{1}{6}[1+2\cos(\tilde{B}t)]\langle S^2\rangle=\mathcal{C}_{11}(t)+\mathcal{C}_{12}(t). \tag{25}$$

V. FOURIER TRANSFORMS

A. Quantum spins

The Fourier transform $\tilde{\mathcal{C}}_{11}(\omega)$ of the real part of the autocorrelation function $\mathcal{C}_{11}(t)$ for the quantum dimer of spin-S spins is given by

$$\tilde{\mathcal{C}}_{11}(\omega)=\sum_{i=0}^{6S+1}f_{S,i}[\delta(\omega-\omega_{S,i})+\delta(\omega+\omega_{S,i})]. \tag{26}$$

The discrete mode frequencies $\omega_{S,i}$ and their amplitudes $f_{S,i}$ are given for $S=1/2$ and $S=5/2$ in Tables II and III in the Appendix.

B. Classical spins

In order to compare the quantum and classical results, it is useful to evaluate the Fourier transform $\tilde{\mathcal{C}}_{11}(\omega)=\int_{-\infty}^{\infty}dt\exp(i\omega t)\mathcal{C}_{11}(t)$ of the classical autocorrelation function. Letting $\tilde{\omega}=\omega/|J|$ and $\overline{B}=\tilde{B}/|J|$, we find for positive ω that

$$\tilde{\mathcal{C}}_{11}(\omega)=\delta(\tilde{\omega})C_{00}+\delta(\tilde{\omega}-\overline{B})C_{01}+\delta\tilde{\mathcal{C}}_{11}(\tilde{\omega}). \tag{27}$$

Exact expressions for the discrete amplitudes C_{00} and C_{01}, and for the continuous part $\delta\tilde{\mathcal{C}}_{11}(\tilde{\omega})$ are given in the Appendix. Then, in order to check the numerical evaluation of the above quantities, we employ the frequency sum rule, $1=\int_0^{\infty}d\omega\tilde{\mathcal{C}}_{11}(\omega)/\pi$.

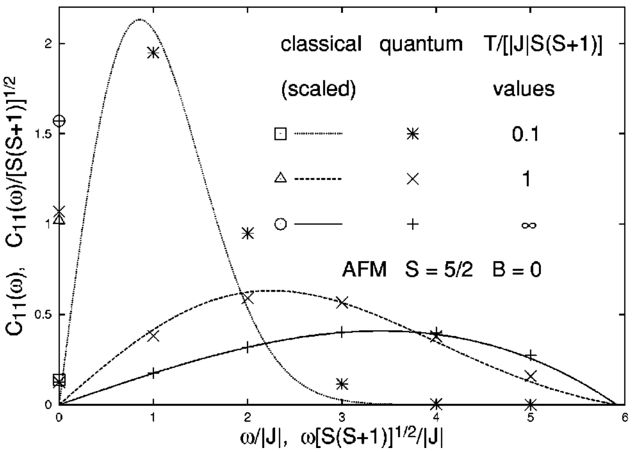

FIG. 5. Plots of the AFM quantum $S=5/2$ modes of $\widetilde{\mathcal{C}}_{11}$ versus $\omega/|J|$ at $\overline{B}=0$ at $\overline{T}=k_BT/[|J|S(S+1)]=0.1,1,\infty$, and for the combined discrete classical modes at $\omega=0$. The curves represent $\delta\widetilde{\mathcal{C}}_{11}(\omega)/[S(S+1)]^{1/2}$ versus $\omega[S(S+1)]^{1/2}/|J|$.

We note that C_{00} also appears in the expression for $\widetilde{\mathcal{C}}_{11}(\omega)$ with $\omega\leqslant 0$. The coefficients C_{00} and C_{01} of the delta functions at $\omega=0$ and $\widetilde{\omega}=\overline{B}$, respectively, are functions of both α and $\overline{B}$. These quantities arise from the long-time rms limit of $\mathcal{C}_{11}(t)$ and for the long-time oscillatory behavior at the driving frequency, respectively. This second δ-function occurs at the resonant frequency in an EPR experiment.

VI. NUMERICAL RESULTS

A. Autocorrelation function spectra

In Fig. 5, we plot the amplitudes $f_{5/2,i}$ of the δ-function modes of the zero-field quantum $S=5/2$ AFM $\widetilde{\mathcal{C}}_{11}(\omega)$ for positive $\omega/|J|$, at the temperatures $\overline{T}=k_BT/[|J|S(S+1)]=\infty,1,0.1$. The amplitudes of the modes at these three $\overline{T}$ values are indicated by the symbols $+$, $\times$, $*$. For comparison, we also show the results of the zero-field classical calculation $\widetilde{\mathcal{C}}_{11}(\omega)$. For $\overline{B}=0$, both of the δ-function amplitudes C_{00} and C_{01} appear at $\omega=0$, and their combined weight at these $\overline{T}$ values is indicated by the circle, triangle, and square, respectively. In addition, the continuous part $\delta\widetilde{\mathcal{C}}_{11}(\omega)$ is plotted both by scaling its amplitude by $1/[S(S+1)]^{1/2}$ and the frequency by $[S(S+1)]^{1/2}$. This combined scaling allows us to compare with the quantum results, while preserving the area under the curves. For $S=5/2$, this scaling changes the maximum $\widetilde{\omega}=\omega/|J|$ from 2 to $\sqrt{35}\approx 5.91$. We note that as $T\rightarrow\infty$, the quantum and classical delta functions at $\omega=0$ agree exactly, both having the weight $\pi/2$. Also as $T\rightarrow\infty$, the classical $\delta\widetilde{\mathcal{C}}_{11}(\omega)$ forms an envelope for the amplitudes of the quantum delta functions, except for a slight deviation at the larger frequencies. At $\overline{T}=1$, the agreement between the quantum and classical results is also pretty good, although there are deviations at nearly every quantum mode value. These deviations are more pronounced at $\overline{T}=0.1$, but the overall agreement is still rather good.

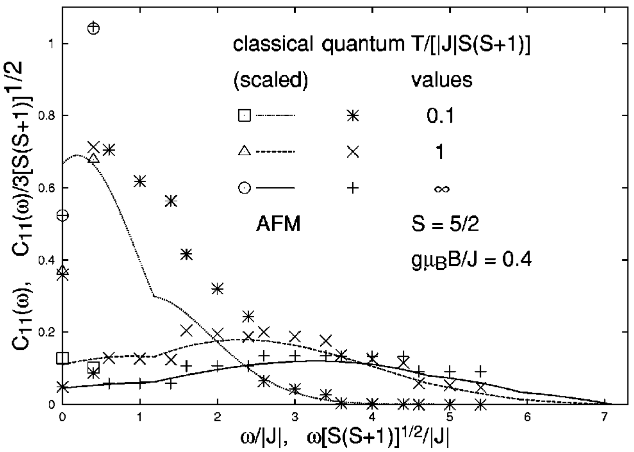

FIG. 6. Plots of the AFM quantum $S=5/2$ modes of $\widetilde{\mathcal{C}}_{11}$ versus $\omega/|J|$ at $\overline{B}=0.4$ at $\overline{T}=0.1,1,\infty$, and for the discrete classical modes at $\omega/|J|=0,\overline{B}$. The curves represent $\delta\widetilde{\mathcal{C}}_{11}/3[S(S+1)]^{1/2}$ versus $\omega[S(S+1)]^{1/2}/|J|$.

In Fig. 6, we show the corresponding curves for the $S=5/2$ AFM dimer at the field $\overline{B}=0.4$. For $\overline{B}\neq 0$, each of the quantum zero-field modes splits into three modes, and therefore to compare the continuous part $\delta\widetilde{\mathcal{C}}_{11}(\omega)$ with the split quantum modes, we divide the scaled continuous part of $\widetilde{\mathcal{C}}_{11}$ by 3, plotting $\delta\widetilde{\mathcal{C}}_{11}/3[S(S+1)]^{1/2}$ versus $\omega[S(S+1)]^{1/2}/|J|$. As in Fig. 5, the classical δ function modes at $\widetilde{\omega}=0,\overline{B}$ are not scaled, but in this case, they are distinct. For this rather strong-field value, $\overline{B}=0.4$, the agreement between the classical and quantum results is very good as $T\rightarrow\infty$, and pretty good at the intermediate $\overline{T}=1$. However, at $\overline{T}=0.1$, these results can differ by more than a factor of two. We note that the classical curves are piecewise continuous functions of ω, with several discontinuities in slope evident. These discontinuities in slope generally appear at the the frequencies corresponding to rather large jumps in the quantum mode amplitude values. At $\overline{T}$ values lower than those pictured, the classical curves develop into three distinct modes with finite widths.

In Figs. 7 and 8, we show the results for the FM $S=5/2$ case at $\overline{B}=0,0.1$, respectively. Choosing $\overline{B}=0.1$ in Fig. 8 allows us to display all of the results clearly on the same figure. Except for the different $\overline{B}$ values in Figs. 8 and 6, Figs. 7 and 8 correspond precisely to Figs. 5 and 6, with the same scaling of the continuous part of the Fourier transform of the classical correlation function, and the same symbols and linestyles. For the FM case at $\overline{B}=0,0.1$, Figs. 7 and 8 show that the agreement between the classical and quantum modes is excellent as $T\rightarrow\infty$, pretty good at $\overline{T}=1$, but only qualitative at $\overline{T}=0.1$. In this case, the classical δ function at $\omega=0$ differs significantly from the quantum one, and the continuous classical curve cannot be scaled in this way at all. As shown for the equivalent neighbor model, the FM classical curves obey a different low-T scaling relation, as the low-T peak center approaches NJ linearly in T from below as $T\rightarrow 0$.[15] In Fig. 8, the development of the continuous classi-

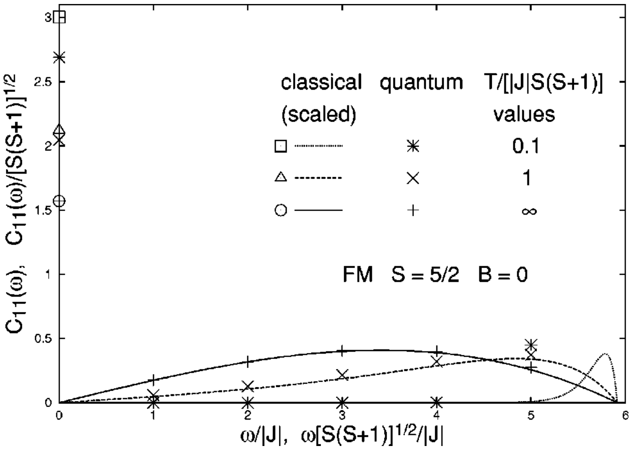

FIG. 7. Plots of the FM quantum $S=5/2$ modes of $\tilde{C}_{11}$ versus $\omega/|J|$ at $\bar{B}=0$ at $\bar{T}=0.1,1,\infty$, and for the combined discrete classical modes at $\omega=0$. The curves represent $\delta\tilde{C}_{11}(\omega)/[S(S+1)]^{1/2}$ versus $\omega[S(S+1)]^{1/2}/|J|$.

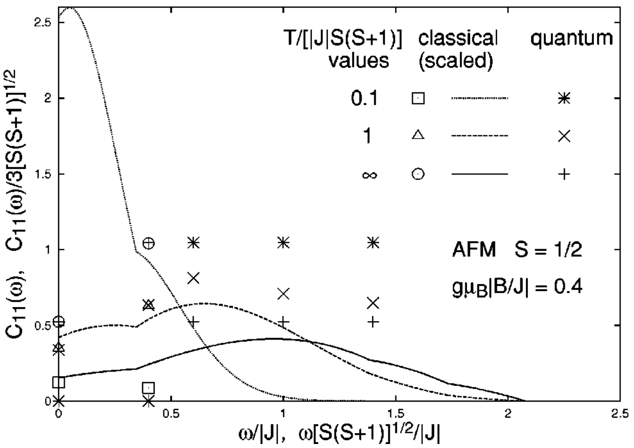

FIG. 9. Plots of the AFM quantum $S=1/2$ modes of $\tilde{C}_{11}$ versus $\omega/|J|$ at $\bar{B}=0.4$ at $\bar{T}=0.1,1,\infty$, and for the discrete classical modes at $\omega/|J|=0,\bar{B}$. The curves represent $\delta\tilde{C}_{11}/3[S(S+1)]^{1/2}$ versus $\omega[S(S+1)]^{1/2}/|J|$.

cal curve into three low T modes is evident, but the fit to the quantum case at $\bar{T}=0.1$ is not good at all. Not only should the low-T classical curves require a different scaling relation, similar to those for $B=0$, the order of the relative heights of the three largest modes at the largest frequencies pictured for the classical curves is inverted relative to that for the quantum case.

We now consider the case $S=1/2$. For the $B=0$ AFM and FM cases, there are two quantum modes for $0\leqslant\omega$, at $\omega/|J|=0,1$. As $T\rightarrow\infty$, these modes have equal intensity $(\pi/2)$, for both FM and AFM cases. For the AFM case as T decreases to 0, the amplitudes of the modes at $\omega/|J|=0(1)$ decrease (increase) continuously to 0 (π), respectively. For the FM case, however, these mode amplitude values increase (decrease) with decreasing T to $2\pi/3$ $(\pi/3)$, respectively, at $T=0$. Somewhat surprisingly, for the AFM case, the amplitude of the combined classical delta functions at $\omega=0$ closely tracks that of the quantum $\omega=0$ mode. For the FM case, however, this tracking is not so good. However, the best that can be said for the continuous part is that as $T\rightarrow\infty$, the second quantum mode nearly falls upon the classical curve scaled as in Figs. 5 and 7, for both AFM and FM cases. At $\bar{T}=k_BT/[|J|S(S+1)]=1,0.1$, this agreement becomes increasingly much worse, respectively. For the FM case, the classical treatment fails miserably as $T\rightarrow 0$, as the amplitude of the classical δ function mode at $\omega=0$ approaches π, and the integrated intensity of the continuous classical mode peak vanishes as $T\rightarrow 0$. Hence, the classical treatment does not describe the $S=1/2$ dimer at $B=0$ correctly, and the correct quantum treatment leads to just two modes for $\omega\geqslant 0$.

For $B\neq 0$, however, there are five modes for $\omega\geqslant 0$ with $S=1/2$, so a classical treatment can approximate the quantum behavior a bit better than for $B=0$. In Figs. 9 and 10,

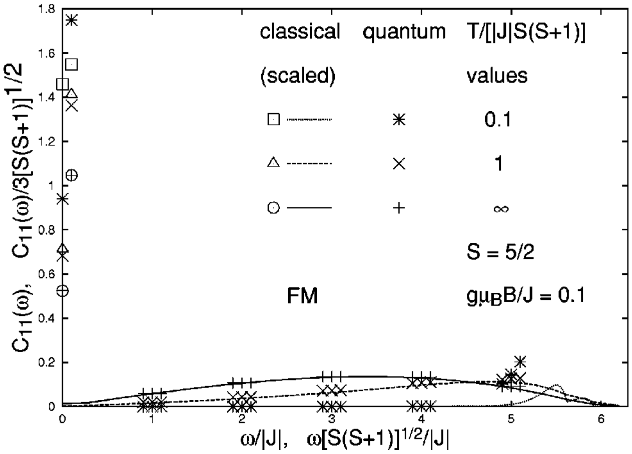

FIG. 8. Plots of the FM quantum $S=5/2$ modes of $\tilde{C}_{11}$ versus $\omega/|J|$ at $\bar{B}=0.1$ at $\bar{T}=0.1,1,\infty$, and for the discrete classical modes at $\omega/|J|=0,\bar{B}$. The curves represent $\delta\tilde{C}_{11}/3[S(S+1)]^{1/2}$ versus $\omega[S(S+1)]^{1/2}/|J|$.

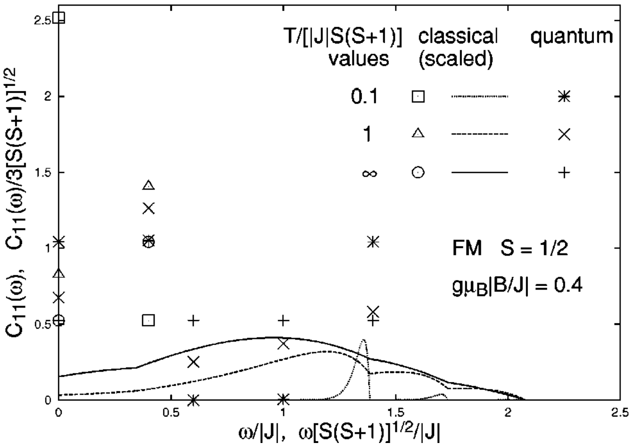

FIG. 10. Plots of the FM quantum $S=1/2$ modes of $\tilde{C}_{11}$ versus $\omega/|J|$ at $\bar{B}=0.4$ at $\bar{T}=0.1,1,\infty$, and for the discrete classical modes at $\omega/|J|=0,\bar{B}$. The curves represent $\delta\tilde{C}_{11}/3[S(S+1)]^{1/2}$ versus $\omega[S(S+1)]^{1/2}/|J|$.

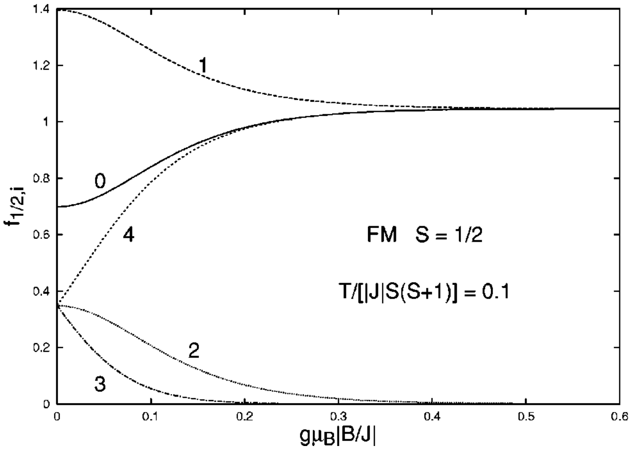

FIG. 11. Plots of the FM quantum $S=1/2$ mode amplitudes $f_{1/2,i}$ versus $\overline{B}$ at $\overline{T}=0.1$ The numerical labels correspond to the i values in Table I of the Appendix.

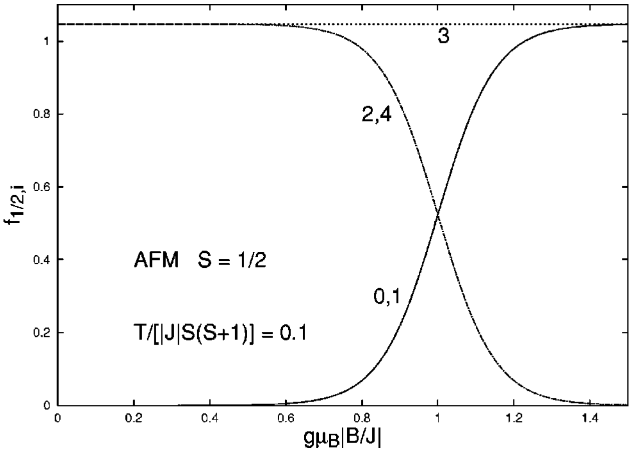

FIG. 12. Plots of the AFM quantum $S=1/2$ mode amplitudes $f_{1/2,i}$ versus $\overline{B}$ at $\overline{T}=0.1$. The mode i values correspond to Table I in the Appendix.

the AFM and FM $S=1/2$ results for $\overline{B}=0.4$ at $\overline{T}=0.1,1,\infty$ are shown. In both cases, the two quantum modes for $\omega/|J|=0,\overline{B}=0.4$ are compared with the two classical delta functions, and the remaining three quantum modes for $0\leqslant\omega$ are compared with the continuous classical curves. In both cases, as $T\rightarrow\infty$, the five quantum modes have the amplitudes $\pi/6$, $\pi/3$, $\pi/6$, $\pi/6$, and $\pi/6$, respectively. The classical results agree precisely with the first two, and form a qualitative envelope similar to the remaining three quantum modes. This agreement is qualitatively preserved at $\overline{T}=1$. However, as $T\rightarrow 0$, the classical and quantum cases differ dramatically. For the AFM case pictured in Fig. 9, the five quantum modes for $0\leqslant\omega$ approach the amplitudes 0, 0, $\pi/3,\pi/3$, and $\pi/3$ as $T\rightarrow 0$, respectively, and the continuous classical curve develops a strong peak at $\omega=0$, which is qualitatively different. The qualitative behavior of the two discrete classical AFM modes is not too bad, however. For the FM case pictured in Fig. 10, as $T\rightarrow 0$, the quantum FM modes approach the amplitudes $\pi/3,\pi/3,0,0$, and $\pi/3$, respectively. That is, the modes at $\omega=0$, $|J+\tilde{B}|$ increase, the modes at $\omega=|J|$, $|J-\tilde{B}|$ decrease, and the mode at $\omega=\tilde{B}$ has a nonmonotonic T dependence. The classical treatment preserves these FM features only qualitatively, and is inaccurate for $\overline{T}\leqslant 0.1$.

B. Field dependencies of the quantum modes

In Fig. 11, we plotted the amplitudes $f_{1/2,i}$ of the five FM quantum modes for $S=1/2$ at $\overline{T}=0.1$ versus $\overline{B}$. The modes $\omega_{1/2,i}$ for $i=0,\ldots,4$ correspond to $\omega=0$, $|\tilde{B}|$, $|J|$, $|J-\tilde{B}|$, and $|J+\tilde{B}|$, respectively. Note that at $B=0$, the $\omega_{1/2,i}$ for $i=0,1$ are degenerate but unequal in intensity, and the $\omega_{1/2,i}$ for $i=2,3,4$ are both degenerate and equal in intensity. At each field, the sum of the five intensities is π. From this figure, it is evident that the crossover from the low-field regime to the high-field regime occurs at the rather low-field value, $\overline{B}\approx 0.1$. The high-field regime is clearly consistent with the mode amplitudes at $\overline{B}=0.4$ pictured in Fig. 10, with the amplitudes of the modes at $\omega/|J|=0,0.4,0.6,1$, and 1.4 approximately equal to $\pi/3,\pi/3,0,0$, and $\pi/3$, respectively.

In Fig. 12, we plotted the amplitudes $f_{1/2,i}$ of the five AFM quantum modes for $S=1/2$ at the $\overline{T}=0.1$. From Fig. 12, the five modes are difficult to discern clearly, due to the strong degeneracies involved. Clearly, the crossover from the low-field to the high-field regime occurs at $\overline{B}=1$. In the low-field regime, the modes at $\omega=0,\tilde{B}$ have nearly zero amplitudes, and the modes with $\omega=|J|,|J\pm\tilde{B}|$ have nearly equal amplitude $\pi/3$. This is the situation pictured for $\overline{B}=0.4$ in Fig. 9. However, Fig. 12 indicates that dramatic changes in the mode amplitudes at low T should take place as $\overline{B}$ is increased from ≈ 0.8 to ≈ 1.2. Over this field range, the amplitudes of the modes at $\omega=|J|,|J+\tilde{B}|$ decrease from nearly $\pi/3$ to nearly 0, and the amplitudes of the modes at $\omega=0,\tilde{B}$ increase from nearly zero to nearly $\pi/3$. Meanwhile, the amplitude of the remaining mode at $\omega=|J|$ remains constant at $\pi/3$. Although not pictured for brevity, at $\overline{T}=1$, all five AFM modes for $S=1/2$ are clearly evident, and the crossover from the weak-field regime to the strong-field regime occurs at $\overline{B}\approx 1.5$.

The field dependencies of the most important modes for the FM and AFM $S=5/2$ dimers are shown at the rather low temperature $\overline{T}=0.1$ in Figs. 13 and 14, respectively. In Fig. 13, the FM modes shown are for $\omega=0$, $\tilde{B}$, $|5J\pm\tilde{B}|$, and $5|J|$. The crossover from the weak- to strong-field limits occurs at about $\overline{B}\approx 0.5$. In the weak-field limit, this corresponds to the dominant modes at $\overline{B}=0.1$ shown in Fig. 8, for which the ranking of the five strongest low-T modes is at $\omega/|J|=0.1,0,5.1,5$, and 4.9, respectively. At high fields, $\overline{B}>2$, there are only three important modes, at $\omega=0,\tilde{B}$, and $5J+\tilde{B}$, which have amplitudes that approach $5\pi/7$, $\pi/7$, and $\pi/7$, at $B\rightarrow\infty$ respectively.

For the AFM case with $S=5/2$, the behavior of the relative mode amplitudes at $\overline{T}=0.1$ is more complicated, as

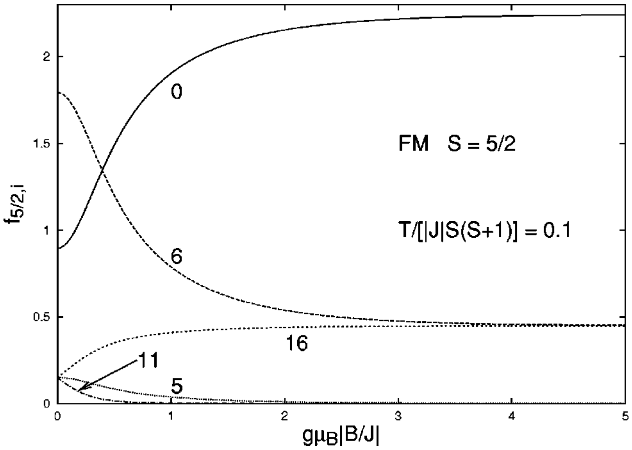

FIG. 13. Plots of the dominant FM quantum $S=5/2$ mode amplitudes $f_{5/2,i}$ versus $\overline{B}$ at $\overline{T}=0.1$. The mode i values correspond to Table II in the Appendix.

shown in Fig. 14. There we plotted the field dependencies of the eight most important modes, which occur at $\omega=0$, $|2J\pm\tilde{B}|$, $2|J|$, $|\tilde{B}|$, $|J\pm\tilde{B}|$, and $|J|$, respectively. From Fig. 14, it is evident that there are essentially three field regimes. The low-field regime occurs for $\overline{B}<0.5$, the intermediate regime is for $1.5<\overline{B}<2.2$, and the high-field regime for $\overline{B}>3$, approximately. An example of the low-field regime at the same temperature was shown for $\overline{B}=0.4$ in Fig. 6. In Figs. 6 and 14, the low-field rank-ordering of the six most important modes are those at $\omega=|\tilde{B}+J|$, $|J|$, $|\tilde{B}-J|$, $|\tilde{B}+2J|$, $2|J|$, and $|\tilde{B}-2J|$, where $J<0$. From the intermediate regime pictured in Fig. 14, however, the two most important modes are those at $\omega=|\tilde{B}+2J|$ and $|\tilde{B}+J|$, with the six other modes in the list contributing lesser, but comparable amounts. Finally, in the high-field regime, the two dominant modes are at $\omega=0$ and $|\tilde{B}|$, respectively.

VII. DISCUSSION

We remark that there have been some experiments on one or more of the Fe2 single molecule magnet dimers. Le Gall *et al.* measured the four Fe2 dimers they made, and found that the zero-field magnetic susceptibility could be fit with the Heisenberg model, with exchange constants ranging from 15 to 19 cm^{-1} (22 to 27 K, which corresponds to $\overline{B}=1$ at $B\approx 16-22$ T). A slightly different fit was made by Lascialfari *et al.*, obtaining $|J|\approx 22K$ for the Fe2 dimer, $[\mathrm{Fe(OMe)(dpm)}_2]_2$.[11] Those authors also refer to EPR measurements that give rise to a zero-field splitting anisotropy of about 7 K in the first excited state, which would complicate the analysis performed here. Such a zero-field splitting would still allow quantum level splitting, but the magnetization steps and the specific heat double peaks would not all be regularly spaced. We remark that these level crossing effects are purely quantum in nature, as the analogous classical calculations do not give rise to such effects, and hence are only approximate for $|\alpha|\gtrsim 1$. Nevertheless, the quantum effects predicted for the magnetization and specific heat ought to be observable with presently available facilities, as one should be able to see one or two magnetization steps, and one or two specific heat double peaks.

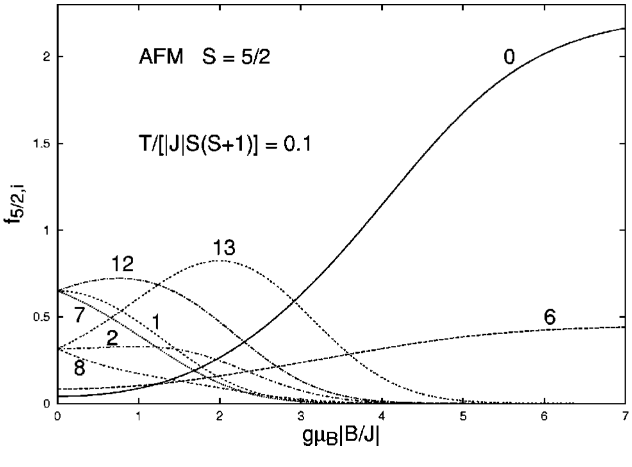

FIG. 14. Plots of the dominant AFM quantum $S=5/2$ mode amplitudes $f_{5/2,i}$ versus $\overline{B}$ at $\overline{T}=0.1$. The mode i values correspond to Table II in the Appendix.

In addition, inelastic neutron scattering would see slightly different results from those presented here. In this situation, the classical envelope curves might be quite useful, as they can serve as a guide to the behavior that might be expected with specific zero-field splitting values. More important, inelastic neutron scattering can be used to probe the details of the magnetic interactions within an individual dimer. Provided that a single crystal of sufficient size for such studies can be obtained, one would perform the experiments at the wave vectors specific to the crystal structure. More precisely, the unpolarized inelastic neutron magnetic dynamical structure factor $S(\mathbf{q},\omega)$ for a single crystal of equal-spin dimers is given by[4,8,16,17]

$$S(\mathbf{q},\omega)=\sum_{\alpha,\beta=1}^{3}(\delta_{\alpha\beta}-\hat{q}_\alpha\hat{q}_\beta)\times\int_{-\infty}^{\infty}\frac{dt}{2\pi}e^{i\omega t}\langle Q_\alpha^{\dagger}(\mathbf{q},t)Q_\beta(\mathbf{q},0)\rangle, \qquad (28)$$

where the $\hat{q}_\alpha=\sin\theta_q\cos\phi_q,\sin\theta_q\sin\phi_q$, and $\cos\theta_q$ for $\alpha=1,2$, and 3, respectively, θ_q, ϕ_q are the angles the scattering wave vector $\mathbf{q}$ makes with the spin quantization coordinates, and $\langle\ldots\rangle$ represents a thermal average, as in Eq. (20). The dimer structure operator

$$Q_\alpha(\mathbf{q},t)=f(\mathbf{q})[e^{i\mathbf{q}\cdot\mathbf{d}}S_{1\alpha}(t)+e^{-i\mathbf{q}\cdot\mathbf{d}}S_{2\alpha}(t)], \qquad (29)$$

where $2\mathbf{d}$ is the displacement vector between the dimer spins, and $f(\mathbf{q})$ is the atomic magnetic form factor.[8,17] The low T, $B=0$ transitions in $S=1/2$ Cu^{2+} and Yb^{3+} and in $S=3/2$ Cr^{3+} dimer powders were treated previously.[8–10] For $\mathbf{B}=0$, the quantization axis is arbitrary, so $\theta_q=\pi/2$ was chosen.[8] For $\mathbf{B}\neq 0$, the quantization axis is parallel to $\mathbf{B}$, so θ_q and ϕ_q are the angles $\mathbf{q}$ makes with the coordinates $\hat{\mathbf{z}}\|\mathbf{B}$ and $\hat{\mathbf{x}}\times\hat{\mathbf{y}}=\hat{\mathbf{z}}$. For scattering wave vectors $\mathbf{q}_c$ directed along the special angle

$$\theta_q^c=\sin^{-1}(2/3)^{1/2}, \qquad (30)$$

the components of each $\widetilde{\mathcal{C}}_{ij}(\omega)$ are sampled equally, and

$$S(\mathbf{q}_c,\omega)=\frac{2}{3\pi}f^2(\mathbf{q}_c)[\widetilde{\mathcal{C}}_{11}(\omega)+\widetilde{\mathcal{C}}_{12}(\omega)\cos(2\mathbf{q}_c\cdot\mathbf{d})] \tag{31}$$

$$=\frac{2}{3}f^2(\mathbf{q}_c)\Bigg[\widetilde{\mathcal{C}}_{11}(\omega)[1-\cos(2\mathbf{q}_c\cdot\mathbf{d})]/\pi + \frac{\cos(2\mathbf{q}_c\cdot\mathbf{d})}{S(S+1)}\Bigg(\langle s_z^2\rangle\delta(\omega)+\frac{1}{2}\langle\mathbf{s}^2-s_z^2\rangle \times[\delta(\omega-\widetilde{B})+\delta(\omega+\widetilde{B})]\Bigg)\Bigg], \tag{32}$$

where we have employed the Fourier transform of the sum rule in Eq. (24). For powder samples, one can still use the special angle technique with a field to obtain $\widetilde{\mathcal{C}}_{11}(\omega)$, but since the direction of **d** is random, one obtains

$$\overline{\cos(2\mathbf{q}_c\cdot\mathbf{d})}=\frac{\sin(2q_cd)}{2q_cd}, \tag{33}$$

where $\overline{\cdots}$ is a spatial average.[17]

For the general case of $\theta_q\neq\theta_q^c$, however, $S(\mathbf{q},\omega)$ cannot be written simply in terms of the $\widetilde{\mathcal{C}}_{ij}(\omega)$. There are four factors h_i for $i=0,\ldots,3$, listed in the Appendix, that depend upon $\mathbf{q}\cdot\mathbf{d}$ and $\sin\theta_q$. We then find

$$S(\mathbf{q},\omega)=\frac{f^2(\mathbf{q})}{2\pi}\sum_{i=1}^{6S+1}f_{S,i}h_{S,i}[\delta(\omega-\omega_{S,i})+\delta(\omega+\omega_{S,i})], \tag{34}$$

where $h_{S,i}$ is the appropriate h_i for the modes $\pm\omega_{Si}$, as indicated for $S=1/2$ and 5/2 in the Appendix. The factors h_0 and h_1 are $\propto\cos^2(\mathbf{q}\cdot\mathbf{d})$, and correspond respectively to the $\omega=0$ and $\pm\widetilde{B}$ modes. The factors h_2 and h_3 are $\propto\sin^2(\mathbf{q}\cdot\mathbf{d})$, and correspond respectively to the modes at $\pm nJ$ and $\pm|nJ\pm\widetilde{B}|$, for $n=1,\ldots,2S+1$. Since h_0 and h_2 are also $\propto\sin^2\theta_q$, whereas h_1 and h_3 are $\propto(1-\frac{1}{2}\sin^2\theta_q)$, the experimenter can fine tune the single crystal data by rotating **B** and **q** relative to **d**.

Neutron powder data on the deuterated $S=1/2$ dimer single molecule magnet $\mathrm{VODPO_4\cdot\frac{1}{2}D_2O}$ ($V2$) were taken, resulting in a fit to the AFM Heisenberg model of $|J|=7.81(4)$ meV,[6] close to the value 7.6 meV found in the susceptibility fit.[18] This corresponds to $\overline{B}=1$ at $B\approx 66$ T, which is too large for thermodynamic studies. However, inelastic neutron scattering at 0.1-0.2$\overline{B}$ ought to be possible for this material. Single crystal data could be particularly interesting. For the Fe2 dimers, inelastic neutron scattering in a field of $\overline{B}\lesssim 0.4-0.5$ should be possible, which would not see any level crossing effects, but could prove interesting, as indicated in Fig. 6.

ACKNOWLEDGMENTS

We thank M. Ameduri and S. E. Nagler for useful discussions. D.E. gratefully acknowledges support from Project No. SFB463 with the MPI-PKS, the MPI-CPfS, the IFW, and the TU Dresden.

APPENDIX

1. Classical time correlation function

From the classical equations of motion,

$$\mathbf{S}(t)=\hat{\mathbf{B}}S_{\parallel}+S_{\perp}[\hat{\mathbf{x}}\cos(\widetilde{B}t)-\hat{\mathbf{y}}\sin(\widetilde{B}t)], \tag{A1}$$

where $\widetilde{B}=\gamma B$, $\hat{\mathbf{B}}$ is a unit vector parallel to **B**, and $\hat{\mathbf{x}}$, and $\hat{\mathbf{y}}$ are orthogonal unit vectors satisfying $\hat{\mathbf{x}}\times\hat{\mathbf{y}}=\hat{\mathbf{B}}$. Since $S_{\parallel}=\mathbf{S}\cdot\hat{\mathbf{B}}$, we have $S_{\parallel}=S\cos\theta$ and $S_{\perp}=S\sin\theta$, and hence $S^2=S_{\parallel}^2+S_{\perp}^2$. $\mathbf{S}_1(t)$ is then found to be

$$S_{1,\parallel}(t)=S_{1,\parallel}+S_{1,\perp}\cos(JSt-\phi_0), \tag{A2}$$

$$S_{1\pm}(t)=e^{\pm i\gamma Bt}\Bigg[\frac{S_{1,\parallel}S_{\perp}}{S_{\parallel}}+\frac{S_{1,\perp}S_{\perp}}{2}\Bigg(\frac{\exp[\mp i(JSt-\phi_0)]}{S_{\parallel}-S}+\frac{\exp[\pm i(JSt-\phi_0)]}{S_{\parallel}+S}\Bigg)\Bigg], \tag{A3}$$

where $S_{1\pm}=S_{1x}\pm iS_{1y}$, and ϕ_0 fixes the initial relative configuration of the two spins. Since $\mathbf{S}_2=\mathbf{S}-\mathbf{S}_1$, we have $S_{1,\parallel}=S_{2,\parallel}=S_{\parallel}/2$ and $S_{1,\perp}=-S_{2,\perp}=(S_{\perp}/S)[1-S^2/4]^{1/2}$. After averaging over ϕ_0,

$$\mathcal{C}_{11}(t)=\frac{1}{4}\Bigg\langle S_{\parallel}^2+2\frac{S_{\perp}^2}{S^2}(1-S^2/4)\cos(SJt)+S_{\perp}^2\cos(\widetilde{B}t)+\frac{(1-S^2/4)}{S^2}\{(S+S_{\parallel})^2\cos[(JS+\widetilde{B})t]+(S-S_{\parallel})^2\times\cos[(JS-\widetilde{B})t]\}\Bigg\rangle. \tag{A4}$$

Replacing S with s for elegance, these classical averages are evaluated from

$$\langle\ldots\rangle=Z^{-1}\int_0^2 sds\int_0^{\pi}\frac{\sin\theta d\theta}{2}e^{\alpha s^2+bs\cos\theta}\ldots, \tag{A5}$$

$$Z=\int_0^2 sds\int_0^{\pi}\frac{\sin\theta d\theta}{2}e^{\alpha s^2+bs\cos\theta}. \tag{A6}$$

The integrals over θ can then be written in terms of $F_0(x)=\sinh(x)/x$ and its first and second derivatives, $F_1(x)=F_0'(x)=[\cosh(x)-\sinh(x)/x]/x$ and $F_2(x)=F_0''(x)=F_0(x)-2F_1(x)/x$, respectively. We note that $F_1(x)/F_0(x)=L(x)=\coth(x)-1/x$ is the Langevin function. We find

$$\mathcal{C}_{11}(t)=\frac{1}{8Z}\int_0^2 s\,ds\,e^{\alpha s^2}\{2s^2G_1(bs,\tilde{B}t)+(4-s^2)\times[\cos(sJt)G_2(bs,\tilde{B}t)+G_3(bs,\tilde{B}t)\sin(sJt)]\}, \tag{A7}$$

$$G_1(x,y)=F_2(x)+[F_0(x)-F_2(x)]\cos(y), \tag{A8}$$

$$G_2(x,y)=F_0(x)-F_2(x)+[F_0(x)+F_2(x)]\cos(y), \tag{A9}$$

$$G_3(x,y)=2F_1(x)\sin(y). \tag{A10}$$

As $T\to\infty$. we set $t^*=|J|t$, and obtain,

$$\lim_{T\to\infty}\mathcal{C}_{11}(t)=\frac{[1+2\cos(\tilde{B}t)]}{6}f(t^*), \tag{A11}$$

$$f(t^*)=1-\frac{[1+2\cos(2t^*)]}{t^{*2}}+\frac{3\sin(2t^*)}{t^{*3}}-\frac{3[1-\cos(2t^*)]}{2t^{*4}}. \tag{A12}$$

We note that $f(t^*)$ was obtained previously for the zero-field case.[19] We also have $\lim_{T\to\infty}\mathcal{C}_{12}(t)=1-\lim_{T\to\infty}\mathcal{C}_{11}(t)$. These forms clearly satisfy the requirement $\lim_{T\to\infty}\mathcal{C}_{11}(0)=1$.

2. Quantum frequency spectrum

The Fourier transform $\tilde{\mathcal{C}}_{11}(\omega)$ of the real part of the autocorrelation function $\mathcal{C}_{11}(t)$ for the quantum dimer of spin-S spins is given by

$$\tilde{\mathcal{C}}_{11}(\omega)=\sum_{i=0}^{6S+1}f_{S,i}[\delta(\omega-\omega_{S,i})+\delta(\omega+\omega_{S,i})], \tag{A13}$$

$$f_{S,i}=\pi a_{S,i}/\mathcal{C}^S(b,\alpha). \tag{A14}$$

For both $S=1/2$ and $S=5/2$, $\mathcal{C}^S(b,\alpha)$ is given by

$$\mathcal{C}^S(b,\alpha)=4S(S+1)e^{2S[b-(2S+1)\alpha]}Z. \tag{A15}$$

We note that $D=S(S+1)Z$ and that $\mathcal{C}^S(0,0)=4S(S+1)\times(2S+1)^2$.

The factors h_i that weight the modes in $S(\mathbf{q},\omega)$ given by Eq. (34) can be derived from Eqs. (28) and (29). In Eq. (28), the off-diagonal terms in $S(\mathbf{q},\omega)$ with $\alpha,\beta=1,2$ sum to zero, and the remaining off-diagonal terms all vanish. Hence, we only require the matrix elements

$$\mathcal{M}^{s'm'}_{sm,\alpha}=(1-\hat{q}^2_\alpha)|\langle sm|Q^\dagger_\alpha(\mathbf{q},0)|s'm'\rangle|^2/f^2(\mathbf{q}). \tag{A16}$$

From Eq. (4) and $s_\pm|sm\rangle=A^\pm_{sm}|s,m\pm1\rangle$, where $A^\pm_{sm}=[s(s+1)-m(m\pm1)]^{1/2}$, we write[20]

$$\langle sm|S_{nz}|s'm'\rangle=\delta_{m',m}[m\delta_{s',s}/2+(-1)^{n-1}\times(B_{sm}\delta_{s',s+1}+C_{sm}\delta_{s',s-1})], \tag{A17}$$

TABLE I. Factors h_i that appear in $S(\mathbf{q},\omega)$, Eq. (31), and their associated transition quantum number changes.

i	Δs	Δm	h_i
0	0	0	$\sin^2\theta_q\cos^2(\mathbf{q}\cdot\mathbf{d})$
1	0	±1	$(1-\frac{1}{2}\sin^2\theta_q)\cos^2(\mathbf{q}\cdot\mathbf{d})$
2	±1	0	$\sin^2\theta_q\sin^2(\mathbf{q}\cdot\mathbf{d})$
3	±1	±1	$(1-\frac{1}{2}\sin^2\theta_q)\sin^2(\mathbf{q}\cdot\mathbf{d})$

$$\langle sm|S_{n\pm}|s'm'\rangle=\delta_{m',m\pm1}[A^\pm_{sm}\delta_{s',s}/2+(-1)^{n-1}\times(B^\pm_{sm}\delta_{s',s+1}+C^\pm_{sm}\delta_{s',s-1})], \tag{A18}$$

for $n=1,2$, respectively. We note that $s_z=S_{1z}+S_{2z}$, $s_\pm=S_{1\pm}+S_{2\pm}$. We find

$$\mathcal{M}^{s'm'}_{sm,\alpha}=\delta_{m',m}[\delta_{s',s}m^2h_0+4h_2(B^2_{sm}\delta_{s',s+1}+C^2_{sm}\delta_{s',s-1})]+\delta_{m',m\pm1}\{h_1(A^\pm_{sm})^2\delta_{s',s}/2+2h_3\times[(B^\pm_{sm})^2\delta_{s',s+1}+(C^\pm_{sm})^2\delta_{s',s-1}]\}, \tag{A19}$$

where the h_i and the changes $\Delta s=s'-s$ and $\Delta m=m'-m$ in the matrix elements for which they occur are listed in Table I. For arbitrary S, each of the $h_{S,i}$ is equal to one of the four h_i listed in Table I. For $S=1/2$ and 5/2, the appropriate choices of the h_{Si} are listed in Tables II and III, respectively. We remark that by setting $f(\mathbf{q})=1$ and each of the $h_i=1$, $S(\mathbf{q},\omega)\to\tilde{\mathcal{C}}_{11}(\omega)/(2\pi)$.

a. Quantum frequencies for S=1/2

For $S=1/2$, we have

$$\mathcal{C}^{1/2}(b,\alpha)=3(1+e^b+e^{2b}+e^{b-2\alpha}), \tag{A20}$$

The mode frequencies $\omega_{1/2,i}$, their relative amplitudes $a_{1/2,i}$, and the factors $h_{1/2,i}$ appearing in $S(\mathbf{q},\omega)$ are given in Table II.

b. Quantum frequencies for S=5/2

For simplicity, we set

$$A_s(b)=\frac{(2s+1)\sinh[(2s+1)b/2]}{\sinh(b/2)}, \tag{A21}$$

TABLE II. Frequency $\omega_{S,i}$ and weighting factor $h_{S,i}$ spectra of the $S=1/2$ Heisenberg dimer in a magnetic field.

i	$\omega_{1/2,i}$	$h_{1/2,i}$	$a_{1/2,i}$
0	0	h_0	$1+e^{2b}$
1	$\lvert\tilde{B}\rvert$	h_1	$(1+e^b)^2$
2	$\lvert J\rvert$	h_2	$e^b(1+e^{-2\alpha})$
3	$\lvert J-\tilde{B}\rvert$	h_3	$e^b(e^b+e^{-2\alpha})$
4	$\lvert J+\tilde{B}\rvert$	h_3	$1+e^{b-2\alpha}$

TABLE III. Frequency $\omega_{S,i}$ and weighting factor $h_{S,i}$ spectra of the $S=5/2$ Heisenberg dimer in a magnetic field.

i	$\omega_{5/2,i}$	$h_{5/2,i}$	$a_{5/2,i}$
0	0	h_0	$2e^{5(b-6\alpha)}\Sigma_{n=1}^{2S}e^{\alpha n(n+1)}\Sigma_{s=1}^{n}s^2\cosh(sb)$
1	$\|J\|$	h_2	$\frac{35}{3}(1+e^{-2\alpha})e^{5b-28\alpha}$
2	$2\|J\|$	h_2	$\frac{32}{15}e^{5b-24\alpha}(1+e^{-4\alpha})\Sigma_{s=0}^{1}A_s(b)$
3	$3\|J\|$	h_2	$\frac{27}{35}e^{5b-18\alpha}(1+e^{-6\alpha})\Sigma_{s=0}^{2}A_s(b)$
4	$4\|J\|$	h_2	$\frac{140}{441}e^{5b-10\alpha}(1+e^{-8\alpha})\Sigma_{s=0}^{3}A_s(b)$
5	$5\|J\|$	h_2	$\frac{1}{9}(1+e^{-10\alpha})e^{5b}\Sigma_{s=0}^{4}A_s(b)$
6	$\|\tilde{B}\|$	h_1	$2\coth(b/2)e^{5(b-6\alpha)}\Sigma_{n=1}^{2S}e^{\alpha n(n+1)}\Sigma_{s=1}^{n}s\sinh(sb)$
7	$\|\tilde{B}+J\|$	h_3	$\frac{35}{3}(1+e^{b-2\alpha})e^{4b-28\alpha}X_1(b)$
8	$\|\tilde{B}+2J\|$	h_3	$\frac{32}{15}e^{3b-24\alpha}(1+e^{b-4\alpha})X_2(b)$
9	$\|\tilde{B}+3J\|$	h_3	$\frac{27}{35}e^{2b-18\alpha}(1+e^{b-6\alpha})X_3(b)$
10	$\|\tilde{B}+4J\|$	h_3	$\frac{140}{441}e^{b-10\alpha}(1+e^{b-8\alpha})X_4(b)$
11	$\|\tilde{B}+5J\|$	h_3	$\frac{1}{9}(1+e^{b-10\alpha})X_5(b)$
12	$\|\tilde{B}-J\|$	h_3	$\frac{35}{3}e^{5b-28\alpha}(e^b+e^{-2\alpha})Y_1(b)$
13	$\|\tilde{B}-2J\|$	h_3	$\frac{32}{15}e^{6b-24\alpha}(e^b+e^{-4\alpha})Y_2(b)$
14	$\|\tilde{B}-3J\|$	h_3	$\frac{27}{35}e^{7b-18\alpha}(e^b+e^{-6\alpha})Y_3(b)$
15	$\|\tilde{B}-4J\|$	h_3	$\frac{140}{441}e^{8b-10\alpha}(e^b+e^{-8\alpha})Y_4(b)$
16	$\|\tilde{B}-5J\|$	h_3	$\frac{1}{9}e^{9b}(e^b+e^{-10\alpha})Y_5(b).$

$$X_s(b)=\frac{e^{-b/2}}{4\sinh^3(b/2)}[e^{sb}\sinh(sb)-s\sinh(b)-4s^2\sinh^2(b/2)], \tag{A22}$$

$$Y_s(b)=X_s(-b)=\frac{e^{b/2}}{4\sinh^3(b/2)}[e^{-sb}\sinh(sb)-s\sinh(b)+4s^2\sinh^2(b/2)]. \tag{A23}$$

We note that $X_1(b)=Y_1(b)=1$ and that $X_s(0)=Y_s(0)=s(4s^2-1)/3$. The mode frequencies $\omega_{5/2,i}$, their relative amplitudes $a_{5/2,i}$, and the $h_{5/2,i}$ factors are given in Table III. In evaluating the coefficients $a_{5/2,i}$ at $\alpha=b=0$, it is useful to employ the relations

$$\sum_{n=1}^{2S}\sum_{s=1}^{n}s^2=\frac{S(S+1)(2S+1)^2}{3}, \tag{A24}$$

$$\sum_{s=0}^{n}(2s+1)^2=\frac{(n+1)(2n+1)(2n+3)}{3} \tag{A25}$$

3. Classical frequency spectrum

From Eq. (27) and letting $\tilde{\omega}=\omega/J$ and $\bar{B}=\tilde{B}/J$, the classical spin Fourier transform $\tilde{\mathcal{C}}_{11}(\omega)$ has the following discrete and continuous contributions,

$$\tilde{\mathcal{C}}_{11}(\omega)=\delta(\tilde{\omega})C_{00}+\delta(\tilde{\omega}-\bar{B})C_{01}+\delta\tilde{\mathcal{C}}_{11}(\tilde{\omega}), \tag{A26}$$

$$\delta\tilde{\mathcal{C}}_{11}(\tilde{\omega})=\sum_{i=1}^{4}C_i(\tilde{\omega}), \tag{A27}$$

$$C_{00}=\frac{\pi}{4Z|J|}\int_0^2 s^3 ds e^{\alpha s^2}F_2(bs), \tag{A28}$$

$$C_{01}=\frac{\pi}{4Z|J|}\int_0^2 s^3 ds e^{\alpha s^2}[F_0(bs)-F_2(bs)], \tag{A29}$$

$$C_1(\tilde{\omega})=\frac{\pi}{4Z|J|}\Theta(2-\tilde{\omega})2\tilde{\omega}(1-\tilde{\omega}^2/4)e^{\alpha\tilde{\omega}^2}\times[F_0(b\tilde{\omega})-F_2(b\tilde{\omega})], \tag{A30}$$

$$C_2(\tilde{\omega})=\frac{\pi}{4Z|J|}\Theta(2-\bar{B}-\tilde{\omega})(\tilde{\omega}+\bar{B})[1-(\tilde{\omega}+\bar{B})^2/4]\times e^{\alpha(\tilde{\omega}+\bar{B})^2}\{F_0[b(\tilde{\omega}+\bar{B})]+F_2[b(\tilde{\omega}+\bar{B})]+2F_1[|b|(\tilde{\omega}+\bar{B})]\}, \tag{A31}$$

$$C_3(\tilde{\omega})=\frac{\pi}{4Z|J|}\Theta(\bar{B}-\tilde{\omega})\Theta(\tilde{\omega}+2-\bar{B})(\bar{B}-\tilde{\omega})\times[1-(\tilde{\omega}-\bar{B})^2/4]e^{\alpha(\bar{B}-\tilde{\omega})^2}\{F_0[b(\bar{B}-\tilde{\omega})]+F_2[b(\bar{B}-\tilde{\omega})]+2F_1[|b|(\bar{B}-\tilde{\omega})]\}, \tag{A32}$$

$$C_4(\tilde{\omega})=\frac{\pi}{4Z|J|}\Theta(\tilde{\omega}-\bar{B})\Theta(2+\bar{B}-\tilde{\omega})(\tilde{\omega}-\bar{B})\times e^{\alpha(\tilde{\omega}-\bar{B})^2}\{F_0[b(\tilde{\omega}-\bar{B})]+F_2[b(\tilde{\omega}-\bar{B})]-2F_1[|b|(\tilde{\omega}-\bar{B})]\}. \tag{A33}$$

4. Low temperature classical modes

We now investigate the low-T behavior of the various contributions $C_i(\omega)$ to the classical $\tilde{\mathcal{C}}_{11}(\omega)$. We follow the procedure used for the isosceles triangle and equivalent neighbor models in zero field. (Refs. 15 and 21)

The FM modal spectrum as $T\to 0$ is given by

$$\Omega_1(\bar{B})=|\bar{B}-2|, \tag{A34}$$

$$\Omega_2(\bar{B})=2, \tag{A35}$$

$$\Omega_3(\bar{B})=\bar{B}+2. \tag{A36}$$

We note that C_1 leads to Ω_2, C_2, and C_3 combine to create Ω_1, and C_4 leads to Ω_3.

As $T\to 0$, the AFM mode frequencies satisfy

$$\Omega_1(\bar{B})=0\Theta(2-\bar{B})+(\bar{B}-2)\Theta(\bar{B}-2), \tag{A37}$$

$$\Omega_2(\bar{B})=\bar{B}\Theta(2-\bar{B})+2\Theta(\bar{B}-2), \tag{A38}$$

$$\Omega_3(\bar{B})=2\bar{B}\Theta(2-\bar{B})+(\bar{B}+2)\Theta(\bar{B}-2). \tag{A39}$$

In $\Omega_1(\bar{B})$, the 0 indicates that the maximum of the mode is at $\tilde{\omega}=0$, the same position as for C_{00}.

[*] Electronic address: efremov@mpipks-dresden.mpg.de
[†] Electronic address: rklemm@mpipks-dresden.mpg.de

[1] D. Gatteschi, A. Caneschi, L. Pardi, and R. Sessoli, Science **265**, 1054 (1994).

[2] A. Lascialfari, D. Gatteschi, F. Borsa, and A. Cornia, Phys. Rev. B **55**, 14 341 (1997).

[3] M.-H. Julien, Z.H. Jang, A. Lascialfari, F. Borsa, M. Horvatić, A. Caneschi, and D. Gatteschi, Phys. Rev. Lett. **83**, 227 (1999).

[4] R. Caciuffo, G. Amoretti, A. Murani, R. Sessoli, A. Caneschi, and D. Gatteschi, Phys. Rev. Lett. **81**, 4744 (1998).

[5] Y. Furukawa, A. Iwai, K. Kumagai, and A. Yakubovsky, J. Phys. Soc. Jpn. **65**, 2393 (1996).

[6] D.A. Tennant, S.E. Nagler, A.W. Garrett, T. Barnes, and C.C. Torardi, Phys. Rev. Lett. **78**, 4998 (1997).

[7] A.W. Garrett, S.E. Nagler, D.A. Tennant, B.C. Sales, and T. Barnes, Phys. Rev. Lett. **79**, 745 (1997).

[8] A. Zheludev, G. Shirane, Y. Sasago, M. Hase, and K. Uchinokura, Phys. Rev. B **53**, 11 642 (1996).

[9] H.U. Güdel, A. Furrer, and H. Blank, Inorg. Chem. **29**, 4081 (1990); H.U. Güdel, Neutron News **7**, 24 (1996).

[10] H.U. Güdel, A. Furrer, W. Bührer, and B. Hälg, Surf. Sci. **106**, 432 (1981).

[11] A. Lascialfari, F. Tabak, G.L. Abbati, F. Borsa, M. Corti, and D. Gatteschi, J. Appl. Phys. **85**, 4539 (1999).

[12] F. Le Gall, F. Fabrizi de Biani, A. Caneschi, P. Cinelli, A. Cornia, A.C. Fabretti, and D. Gatteschi, Inorg. Chim. Acta **262**, 123 (1997).

[13] D. Mentrup, J. Schnack, and M. Luban, Physica A **272**, 153 (1999).

[14] R. Klemm and M. Luban, Phys. Rev. B **64**, 104424 (2001); cond-mat/0105050 (unpublished).

[15] R.A. Klemm and M. Ameduri, Phys. Rev. B **66**, 012403 (2002); cond-mat/0112236 (unpublished).

[16] R. M. White, *Quantum Theory of Magnetism* (McGraw-Hill, New York, 1970), pp. 207–225.

[17] A. Furrer and H.U. Güdel, Phys. Rev. Lett. **39**, 657 (1977).

[18] J.W. Johnson, D.C. Johnston, A.J. Jacobson, and J.F. Brody, J. Am. Chem. Soc. **106**, 8123 (1984).

[19] G. Müller, J. Phys. (Paris) **8**, 1403 (1988).

[20] E. U. Condon and G. H. Shortley, *The Theory of Atomic Spectra* (Cambridge University Press, Cambridge, 1964).

[21] M. Ameduri and R. Klemm, cond-mat/0108213 (unpublished).